JOURNAL OF GEOPHYSICAL RESEARCH, VOL. 101, NO. B4, PAGES 8363–8381, APRIL 10, 1996

Cyclic stressing and seismicity at strongly coupled subduction zones

Mark A. J. Taylor, Gutuan Zheng, and James R. Rice

Division of Applied Sciences and Department of Earth and Planetary Sciences
Harvard University, Cambridge, Massachusetts

William D. Stuart

U.S. Geological Survey, Menlo Park, California

Renata Dmowska

Division of Applied Sciences and Department of Earth and Planetary Sciences
Harvard University, Cambridge, Massachusetts

Abstract. We use the finite element method to analyze stress variations in and near a strongly coupled subduction zone during an earthquake cycle. Deformation is assumed to be uniform along strike (plane strain on a cross section normal to the trench axis), and periodic earthquake slip is imposed consistent with the long-term rate of plate convergence and degree of coupling. Simulations of stress and displacement rate fields represent periodic fluctuations in time superimposed on an average field. The oceanic plate, descending slab, and continental lithosphere are assumed here to respond elastically to these fluctuations, and the remaining mantle under and between plates is assumed to respond as Maxwell viscoelastic. In the first part of the analysis we find that computed stress fluctuations in space and time are generally consistent with observed earthquake mechanism variations with time since a great thrust event. In particular, trench-normal extensional earthquakes tend to occur early in the earthquake cycle toward the outer rise but occur more abundantly late in the cycle in the subducting slab downdip of the main thrust zone. Compressional earthquakes, when they occur at all, have the opposite pattern. Our results suggest also that the actual timing of extensional outer rise events is controlled by the rheology of the shallow aseismic portion of the thrust interface. The second part of the analysis shows the effects of mantle relaxation on the rate of ground surface deformation during the earthquake cycle. Models without relaxation predict a strong overall compressional strain rate in the continental plate above the main thrust zone, with the strain rate constant between mainshocks. However with significant relaxation present, a localized region of unusually low compressional, or even slightly extensional, strain rate develops along the surface of the continental plate above and somewhat inland from the downdip edge of the locked main thrust zone. The low strain rate starts in the middle or late part of the cycle, depending on position. This result suggests that the negligible or small contraction measured on the Shumagin Islands, Alaska, during 1980 to 1991, may not invalidate an interpretation of that region as being a moderately coupled subduction zone. In contrast, mantle relaxation causes only modest temporal nonuniformity of uplift rates in the overriding plate and of extensional stress rates in the subducting plate, even when the Maxwell time is an order of magnitude less than the recurrence interval.

Introduction

Subduction zone seismicity is currently discussed in terms of the degree of coupling or locking of the interface between the subducting oceanic plate and the overriding plate [*Kanamori*, 1971; *Ruff and Kanamori*, 1983]. At strongly coupled subduction zones the interface, called the main thrust zone, appears to have much of its area locked until rupture during a great earthquake, after which the interface locks again. The repeated locking and unlocking amounts to a time varying shear stress condition at the plate interface, perturbing the time-averaged stress field set up by the steady forces that determine overall plate motion.

The observational evidence for periodic stressing of a subducting oceanic plate is temporal variation of focal mechanisms of intraplate earthquakes [*Christensen and Ruff*, 1983, 1988; *Astiz and Kanamori*, 1986; *Astiz et al.*, 1988; *Lay et al.*, 1989]. Near the end of the earthquake cycle, mechanisms of the relatively rare earthquakes that then occur between the outer rise and the bathymetric trench are generally consistent with maximum deviatoric compression in the direction of plate motion; at the far more active intermediate depths of 40 to 200 km in the descending slab

Copyright 1996 by the American Geophysical Union.

Paper number 95JB03561.
0148-0227/96/95JB-03561$05.00

(40 km typically being the bottom of a main thrust zone) the axis of maximum deviatoric extension aligns with the plate motion direction. After the mainshock the pattern is reversed during the first few decades (or longer for the largest earthquakes, e.g., Chile 1960 and Alaska 1964). This reversal usually causes abundant shallow extensional normal faulting toward the outer rise and a diminution of extensional activity, or even a change to compression, at intermediate depths in the descending slab.

To help understand the connection between intraplate seismicity and the mainshock at a subduction zone, we study the variations of stress and deformation within a cycle whose period is defined by two successive earthquake ruptures of the main thrust zone and restrict ourselves to only the case of strongly coupled subduction zones. There are several reasons for this. There are several well studied examples of strongly coupled subduction zones having repeated great earthquakes such as Southern Chile, Alaska, and Japan, among others. Repetition implies some stationarity of the cause of the coupling and helps justify our approximation that main thrust zone earthquakes are periodic. We note, however, that there are no examples of exactly periodic great earthquakes. Another reason is that long along-strike earthquake rupture zones associated with strong coupling justify using a two-dimensional model and omitting along-strike interaction of neighboring earthquakes. Third, strongly coupled zones have the largest stress and deformation variation between successive earthquakes. Any rate-dependent material response, such as relaxation in the mantle or in the shallow aseismic part of the thrust zone adjoining the trench, should then be most apparent, as would its effect on intraplate seismicity and ground surface motion. Indeed, *Dmowska and Lovison* [1992] have recently shown that the seismic manifestations of stress changes, discussed above, are most prevalent adjacent to what (from seismic wave field studies) had been characterized as strongly locked "asperities" along the plate interface. These asperities are regions of highest moment release during the great event and can hence be assumed to be more firmly locked between earthquakes thus inducing the greatest cycle-associated stress fluctuations in their vicinity. (This interpretation is discussed further based on a three-dimensional generalization of the finite element modeling here by *Dmowska et al.* [1996].)

In contrast to strongly coupled subduction zones, the main thrust zone at weakly coupled subduction zones is thought to be divided into a distribution of locked areas (patches) surrounded by aseismic creep. The maximum earthquake size on the main thrust zone is thus likely to be smaller than in the strongly coupled case. Uncoupled subduction zones apparently have patches so small or weak that the main thrust zone slides at essentially constant rate and shear stress, unless perturbed by large earthquakes that rupture through the subducting plate or occur on strongly locked interface zones to the side.

Cycle related seismicity variations in coupled subduction segments and qualitative models of stress transfer are reported by *Christensen and Ruff* [1983, 1986, 1988], *Astiz and Kanamori* [1986], *Astiz et al.* [1988], *Dmowska et al.* [1988], *Dmowska and Lovison* [1988], *Lay et al.* [1989], and *Cohen* [1994]. The model we use is a more detailed quantitative version of the one-dimensional model of *Dmowska et al.* [1988] and can be regarded as an improvement of it, giving a more complete account of the geometry and constitutive properties of the lithosphere and asthenosphere and providing a numerical, two-dimensional, and linear solid mechanics solution. As in the one-dimensional model, our model involves periodic mainshock slip specified as a boundary condition. The resulting stress field is similarly superposed on an unknown steady background field that we do not attempt to estimate here. The periodic slip modulates the steady loading of the main thrust zone caused by deep slab pull and slippage of the oceanic-continental plate interface to the sides of the main thrust zone. Within the assumption that the response to stress fluctuations throughout the cycle is linear elastic or viscoelastic, the stress fluctuations can be computed without knowing the average stress, as shown in general by *Dmowska et al.* [1988] and used by them in the context of their one-dimensional model. Still, since these fluctuations involve perturbations about the average stress field, the rheological parameters governing that linearized fluctuation response would, in a fuller theory, depend on the average stress and temperature. In order to simplify, we merely assume the rheological properties governing such fluctuations, taking them to be elastic in some places and possibly Maxwell viscoelastic in others. Assuming them to be elastic simply means that the Maxwell time is much longer than the recurrence interval.

We note that the designation of weak or strong coupling is an approximate parameterization. In a more comprehensive model, fault slip and stress would satisfy a fault constitutive law, for example, as in the work of *Tse and Rice* [1986] and *Stuart* [1988] and be part of the solution that included all forces affecting subduction. We do not address the fundamental cause of strong or weak coupling at a subduction zone interface. Nor do we allow for precise treatment of any aseismic shear zones downdip of the main thrust zone but instead treat the material as part of the asthenospheric mantle wedge.

The next section explains the details of the model, and the following section presents computed extensional stress histories in the subducting slab for positions near the trench axis and the lower edge of the main thrust zone. Comparison of computed results with stress directions and timing associated with intraplate earthquakes shows general agreement. Finally, we compute strain and uplift at the ground surface over the main thrust zone during an earthquake cycle and compare these results with trends from global subduction zones.

Finite Element Model

The finite element model is two-dimensional with plane strain in a vertical cross section normal to the fault trace (trench axis). This approximation is suitable for subduction zones where the along-strike earthquake rupture is greater than a few times the downdip length and is satisfied by sections of subduction zones having earthquakes of $M > 8$. Figure 1a shows the geometry of the model. There are two elastic lithosphere plates. The oceanic plate spans the model width and dips at angle θ underneath the overriding continental plate in the subduction zone. Both plates have shear modulus μ and Poisson's ratio $\nu = 0.25$ (so that the Lamé constants λ and μ are equal). The oceanic plate has uniform thickness H measured normal to its horizontal or

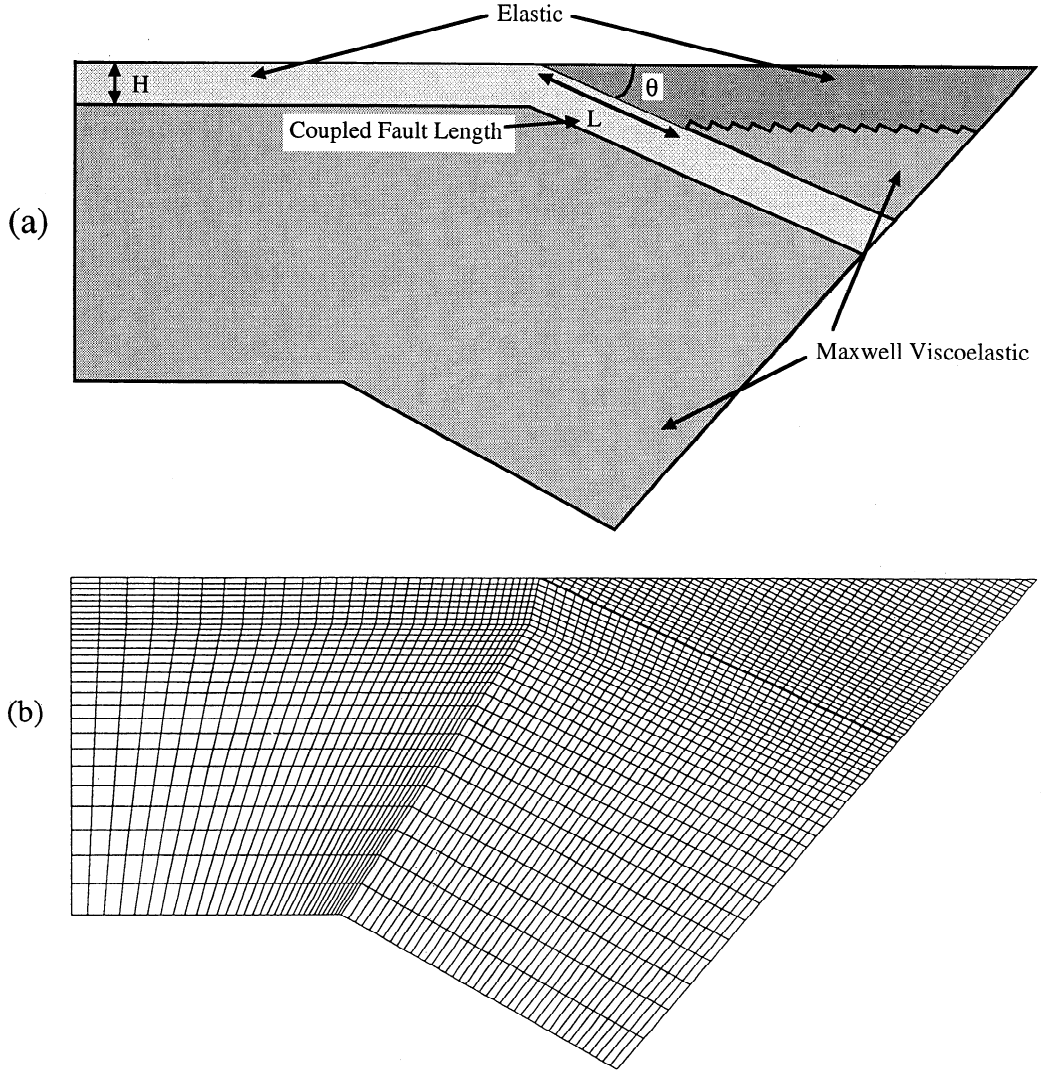

Figure 1. (a) Model geometry showing elastic oceanic plate, elastic continental plate, and viscoelastic mantle. Dip $\theta = 25°$. (b) Finite element mesh is shown.

dipping surface. An asthenospheric region underlies the oceanic plate and also fills the wedge between the overlying continental and subducting oceanic plates. Both asthenosphere volumes are assumed to behave as Maxwell viscoelastic material with rigidity μ, $\nu = 0.25$, and viscosity η. The corresponding material relaxation time is $T_{rel} = \eta/\mu$, referred to as the Maxwell time. Two sets of coordinate axes are set up to conveniently describe the model, both with their origin at the fault trace along the trench (Figure 2). The x-y axes have the x axis coincident with the ground surface, and the ξ–ζ axes have the ξ axis along the top surface of the subducting plate.

The main thrust zone in our model is a thin layer of material extending downdip over a distance L between the oceanic and continental plates where they would otherwise be in contact along $0 \le \xi \le L$. The model main thrust zone represents a fault zone that has large slip and hence large shear strain over the fault thickness during periodic great earthquakes. We consider here cases for which L is 100 km and the width of the plate H is 30, 40, or 50 km. The angle of dip θ of the downgoing slab along portions of subduction zones that produce great earthquakes is usually about 15°-20° from the trench to the bottom of the continental plate and then increases to around 30° [*Jarrard*, 1986]. Though a variable dip would be more realistic, and has been used in specific modeling of the Shumagin Islands, Alaska region by *Zheng et al.* [this issue], a uniform dip is consistent with the other approximations made for the present generic modeling. We consider dip angles of 15°, 20°, 25° and 30°. The Maxwell time T_{rel} is varied as a fraction of the total earthquake cycle time T_{cyc} by changing the viscosity of the material. Values of T_{rel}/T_{cyc} considered are 1/12, 1/6, 1/3, and ∞ (for the elastic case).

The model geometry resembles that of the finite element model of *Melosh and Raefsky* [1983], which has a dipping elastic slab passing through a viscoelastic asthenosphere and terminating in a more resistant viscoelastic mesosphere. Their model is used to study early postseismic relaxation after a single earthquake. *Wahr and Wyss* [1980] also did finite element modeling of deformation and interpret the region below the upper plate as viscoelastic, whereas the analytic models of *Savage* [1983] and *Thatcher and Rundle*

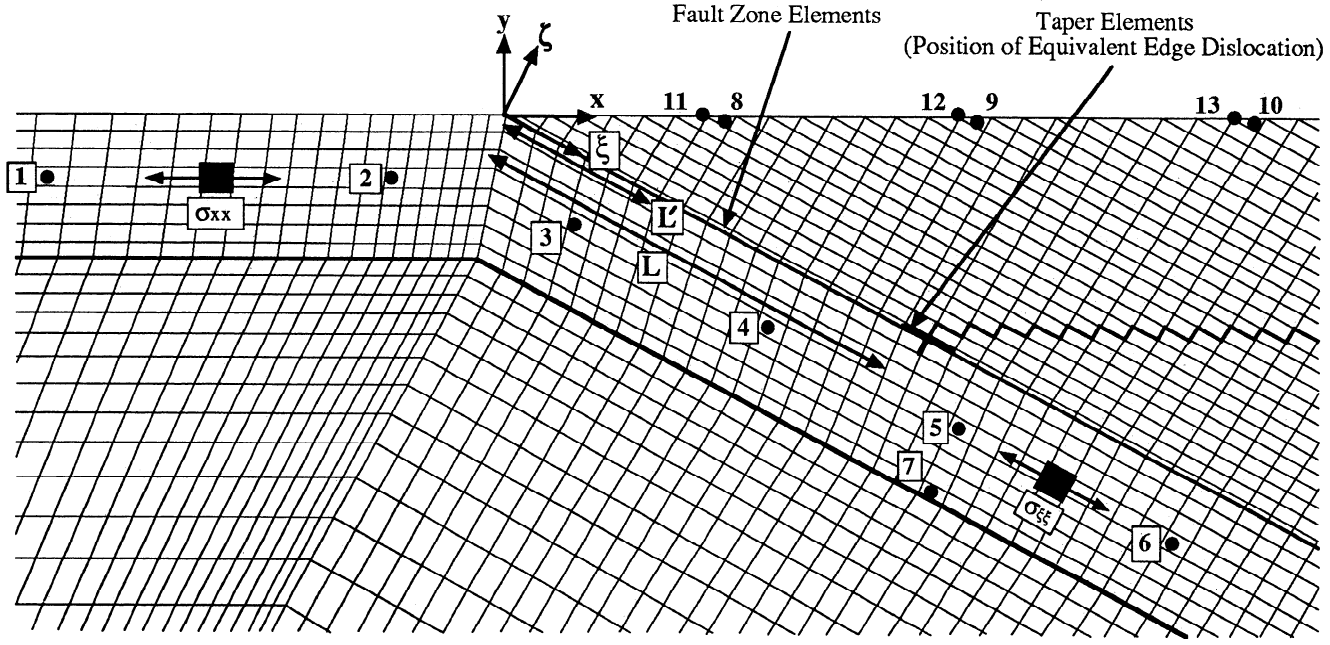

Figure 2. Section of the finite element mesh showing magnified view of thin fault zone elements at interface of oceanic and continental plates and the positions of elements and nodes from which data is taken for the plots. For L = 100 km and H = 30 km, the following is indicated:

1 and 2 are 98 km and 21 km oceanward respectively, 13 km below slab surface

3, 4, 5, and 6 are 25 km, 74 km, 123 km, and 178 km downdip, respectively, 13 km below slab surface;

7 is 123 km downdip, 28 km below slab surface;

8, 9, and 10 are 51 km, 109 km, and 174 km, respectively, along continent surface; and

11, 12, and 13 are 50 km, 108 km, and 173 km, respectively, along continent surface. Edge dislocation symbol at $\xi = L$ represents seismic slip.

[1984b] have a single viscoelastic layer and repeated earthquake cycles but no slab penetration into the asthenosphere.

The finite element mesh, Figure 1b, is assembled of quadrilateral bilinear plane strain elements. Elements that appear to be triangles are degenerate quadrilaterals with a coincident node pair. The side and bottom boundaries of the entire mesh of Figure 1b are sufficiently far from the lower edge of the main thrust zone to make negligible difference in solutions for similar cases of fixed and free remote boundaries. Figure 2 shows a close-up view of the mesh near the main thrust zone. Because of the way we generate the mesh, the layer of thin elements, of which the main thrust zone is the upper part, continues to the right edge of the model. The thin elements along $0 < \xi < L$ constitute the thrust contact zone which remains locked between earthquakes These elements are elastic but are given additional shear "transformation" strains to simulate earthquake slip, as described below. The thin elements on $\xi > L$ belong to the asthenosphere and are Maxwell viscoelastic, generally with Maxwell time $T_{rel} = \eta/\mu$ (*Zheng et al.* [this issue] consider models for the Shumagins with a reduced viscosity in that region to represent an aseismic downdip continuation of the coupled part of the fault zone). In order to mitigate the unphysical stress concentrations at the interface between the two element types, two "taper" elements are assigned at $\xi = L$ to simulate the thermalbased transition from stick slip to stable shearing, as explained below.

Average and Fluctuating Parts of Stress and Displacement Rate

Following *Savage* [1983], *Thatcher and Rundle* [1984a,b], *Dmowska et al.* [1988], *Rundle* [1988a,b] and *Cohen* [1994], we think of the actual total stress and displacement rate fields of the domain σ_{ij}^{tot} and $\dot{u}_i^{tot}$ as superpositions of long term time-averaged fields σ_{ij}^{avg} and $\dot{u}_i^{avg}$ and periodic fluctuations σ_{ij}^{fluct} and $\dot{u}_i^{fluct}$ about the average due to the periodic earthquakes:

$$\begin{aligned} \sigma_{ij}^{tot} &= \sigma_{ij}^{avg}(\mathbf{r}) + \sigma_{ij}^{fluct}(\mathbf{r},t) \\ \dot{u}_i^{tot} &= \dot{u}_i^{avg}(\mathbf{r}) + \dot{u}_i^{fluct}(\mathbf{r},t) \end{aligned} \tag{1}$$

where $\mathbf{r}$ is spatial position.

The average, or steady state, fields represent stress and deformation rate due to the variety of forces that influence long-term plate motion. These include body forces due to density variations, dissipative forces due to long-term viscous flow in the mantle, and plastic deformation within lithosphere plates (bending and slip on other faults). These average fields correspond to an imagined state in which intermittent motion on the thrust interface is replaced by a steady imposed slip rate there, so that there results a steady subducting flow with velocity distribution $\dot{u}_i^{avg}(\mathbf{r})$. The material response in such a flow is viscous in the hotter parts of the system. It will involve partly brittle processes in bending of the cold subducting plate. We ignore that such brittle flow involves finite stress drops on fault

segments as they fail and consider it as brittle creep at constant stress. The description of the time-invariant steady state field is not exact, of course, since the overall configuration of plates on the Earth evolves. Nonetheless, if the averaging time is taken long enough to encompass numerous mainshock ruptures, then such average fields may be defined so that the perturbations σ_{ij}^{fluct} and $\dot{u}_i^{fluct}$ associated with each earthquake cycle average close to zero over a cycle. The perturbation stresses σ_{ij}^{fluct} equilibrate zero body forces, the body forces already being equilibrated by σ_{ij}^{avg}. We assume that linear constitutive relations apply between the fluctuating parts of the stress and strain, σ_{ij}^{fluct} and ε_{ij}^{fluct}. For the timescale of the cyclic fluctuations of the order of 50 to 100 years, only the asthenosphere response to these fluctuations is assumed to be viscoelastic. The response is assumed to be elastic elsewhere.

We let $\Delta^{tot}(\xi,t)$ denote slip along the coupled part of the interplate interface. Our modeling simulates the perturbation fields, which are considered to be driven by a specified periodic part $\Delta^{fluct}(\xi,t)$ of that slip, and is superposed on an average slip $\Delta^{avg}(t)=V_{pl}t$, where V_{pl} is the long-term steady slip rate of relative plate motion. To specify the slip fields in a way that allows for other than ideally strong coupling, it is necessary to introduce a "seismic coupling factor" α ($0 < \alpha \le 1$), the ratio of seismic slip to total slip during a cycle. The motivation for α is the large discrepancy between slip rates determined from a global plate model and the seismic slip rates of different subduction zones. *Pacheco et al.* [1993] have phenomenologically related α to variations in plate convergence rate and age of the downgoing oceanic lithosphere, absolute velocity of the overriding plate in a hotspot reference frame, and differences in the evolutionary stage of subduction. So $\Delta^{fluct}(\xi,t)$ is defined to represent periodic slip of magnitude $\alpha V_{pl}T_{cyc}$ at the time of each earthquake, with recurrence time T_{cyc}, whereas between earthquakes $\Delta^{fluct}(\xi,t)$ decreases at a constant rate $-\alpha V_{pl}$ for simplicity to make for a zero average over time. Thus the total slip can be written

$$\Delta^{tot}(\xi,t)=\Delta^{avg}(t)+\Delta^{fluct}(\xi,t)=V_{pl}t+\Delta^{fluct}(\xi,t)$$
$$\Delta^{fluct}(\xi,t)=[S(t/T_{cyc})+1/2-t/T_{cyc}]\alpha V_{pl}T_{cyc} \quad (2)$$

where $S(t/T_{cyc})$ is a periodic staircase function, rising by unity whenever the argument is an integer and otherwise defined as the integer part of its argument. Figure 3 shows this decomposition of interface slip into steady and periodic functions and the resultant slip behavior, so that within this approximation the total interface slip increases by $\alpha V_{pl}T_{cyc}$ in each earthquake and increases at a uniform rate $(1-\alpha)V_{pl}$ between earthquakes. This provides an approximation which ignores spatial and temporal heterogeneities of slip by lower magnitude seismicity and creep along the interface in the nonideally coupled case. The fluctuating parts σ_{ij}^{fluct} and $\dot{u}_i^{fluct}$ of stress and velocity fields are then directly calculated from the finite element method, with assumed elastic or Maxwell viscoelastic response to the fluctuations, by imposing the periodic slip $\Delta^{fluct}(\xi,t)$ along the thrust zone.

The imposed slip function $\Delta^{fluct}(\xi,t)$ is equivalent to having the core of a time-varying Volterra edge dislocation at position $\xi = L$ and would create a singular stress field in a continuous medium. In the finite element formulation we implement the condition on Δ^{fluct} by imposing an appropriate non-elastic shear strain history on the set of

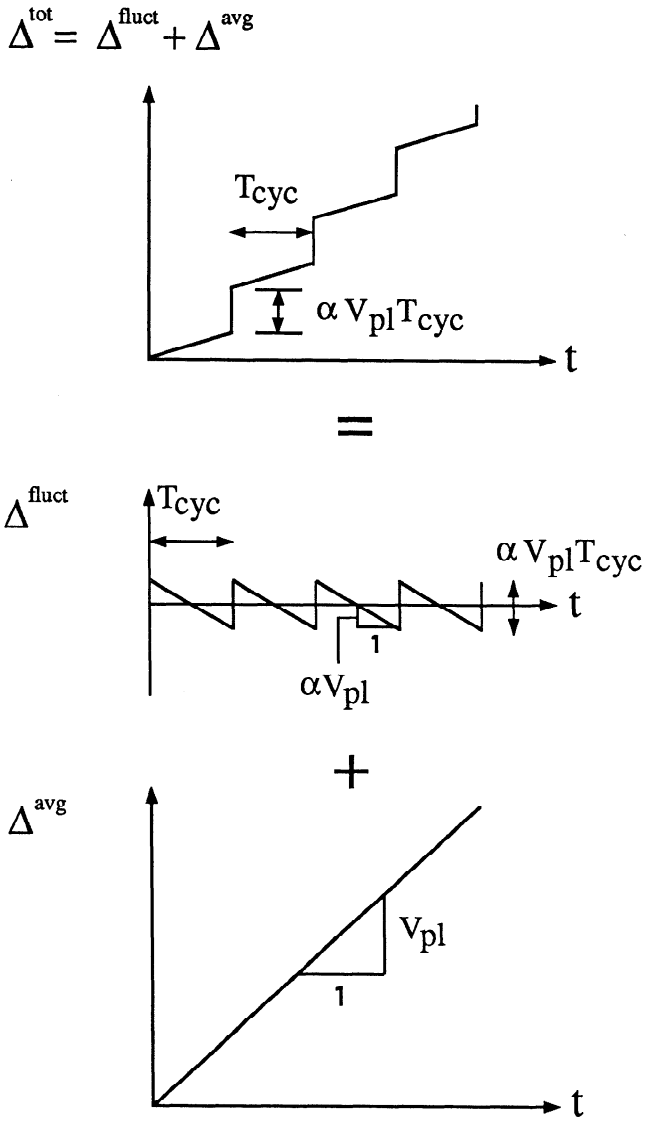

Figure 3. Decomposition of fault slip history. Imposed periodic slip Δ^{fluct} with zero average superposed on the average slip Δ^{avg}.

thin elements that represent the fault zone (Figure 2). Thus the shear component $\varepsilon_{\xi\varsigma}$ of the (tensor) strain within the elements of the coupled fault layer, $0 \le \xi \le L$, has a "transformation" strain $\varepsilon_{\xi\varsigma}^T$ added to its elastic part $\sigma_{\xi\varsigma}/2\mu$ and is thus represented as

$$\varepsilon_{\xi\varsigma}=\frac{\sigma_{\xi\varsigma}}{2\mu}+\varepsilon_{\xi\varsigma}^T \quad (3)$$

where we specify the history of $\varepsilon_{\xi\varsigma}^T$. Specifically, to represent the periodically fluctuating part of the slip corresponding to $\Delta^{fluct}(t)$, we choose $\varepsilon_{\xi\varsigma}^T(t)$ so that $2h\varepsilon_{\xi\varsigma}^T(t)=\Delta^{fluct}(t)$, where h is the thickness of the fault zone. In the finite element solid mechanics code ABAQUS (made available under academic license from Hibbitt, Karlsson and Sorensen, Inc., of Pawtucket, Rhode Island) that we use for all simulations, the fault element transformation strain is specified by adapting the anisotropic thermal strain capability of the code.

To help reduce the zone of poor representation of the stress field by the finite element mesh, we refine the

element mesh near $\xi = L$, where imposed slip terminates. The transformation strain is decreased linearly from its value in the coupled fault zone (which varies with time) to zero over the length of the "taper" elements which join the seismic and aseismic parts of the fault. The material properties of the taper elements are chosen such that the shear modulus μ is reduced by a factor of 100 compared to the modulus in the neighboring fault, but ν is increased to nearly 0.5, so that the bulk modulus K is the same as in the rest of the fault. The elements are made Maxwell viscoelastic with the viscosity η also reduced by 100 to keep the inherent Maxwell time (η/μ) the same as the mantle.

In the following discussion computed results are presented in dimensionless form, for example stress is plotted by showing the variation of $\sigma L/\mu\alpha V_{pl}T_{cyc}$ as a function of x/L or ξ/L. Characteristic dimensional parameters are distance L, cycle time T_{cyc}, and seismic displacement $\alpha V_{pl}T_{cyc}$. A characteristic strain is seismic displacement divided by fault width, $\alpha V_{pl}T_{cyc}/L$, essentially a strain due to the equivalent edge dislocation core at $\xi = L$. Here and subsequently, σ and $\dot{u}$ without superscripts refer to the fluctuating part of the stress and velocity fields, respectively.

We find that for models with linear viscoelastic rheology, periodic response is effectively attained by the third cycle $2T_{cyc} \le t \le 3T_{cyc}$ of simulations (but labeled 0 to T_{cyc} on plots). The first two cycles have minor deviations from later cycles because of initial conditions. Stress and strain values are reported as averages at element centroids, and displacements are calculated at nodes. Since the results are perturbations on an average stress field that is left undetermined in this study, plots are interpreted mainly in terms of rates and rate changes.

Extensional Stress Variation in Subducting Plate

In this section we examine the space and time variation of the extensional stress component $\sigma_{\xi\xi}$ in the descending slab and σ_{xx} in the oceanic floor; stresses are positive when tensile. These stress components are directed along the direction of motion of the subducting plate. Their variation is the main influence on principal stresses that control earthquake mechanisms in the oceanic plate, at least for simple, nonoblique subduction as here, for which the long-term-averaged stresses σ_{ij}^{avg} can reasonably be assumed to have a greatest or least principal direction aligned with the direction of subduction. We focus primarily on a reference case whose parameter values are 25° dip, $T_{rel}/T_{cyc} = 1/6$, and $H/L = 3/10$, but we also summarize results of varying the value of one parameter at a time. Below 200 km depth in the slab, observed earthquakes are generally compressional, probably because of compression due to jamming of the lower end of the slab into more resistive mantle [*Melosh and Raefsky*, 1983]. Because our finite element model does not consider such variable resistance we have considered fluctuating extensional stresses only within a distance $2L$ of the lower edge of the main thrust zone. Histories of stress versus time will be shown subsequently for the set of elements marked 1 to 7 in Figure 2.

To help understand the consequences of relaxation, we first show results for the case of an elastic half-space. This case corresponds to the elastic half-space model of *Savage* [1983], and we obtain results by setting the Maxwell time $T_{rel}/T_{cyc} = \infty$ (elastic asthenospheric response to stress fluctuations). There is then no distinction between properties of the lithosphere and asthenosphere. Computed results are plotted in dimensionless form. Time is expressed as a fraction of the cycle time T_{cyc} and positions along the ξ axis are normalized by L.

Figure 4a shows the variation of $\sigma_{\xi\xi}$ or σ_{xx} along the length of the subducting plate at a depth of about 13 km (for a value for H of 30 km) from the surface of the plate. Each of the six curves is for a different time during the earthquake cycle (the times being chosen to give a good spread of the curves) and times being normalized to T_{cyc}. It can be seen that, broadly speaking, the fluctuating stress changes from tensional to compressional during the cycle in the seafloor toward the outer rise and changes in the opposite sense in a region of length about L in the downgoing slab. Beyond that, the trend is once again from tension to compression, although the magnitude of the overall stress variation is less. In the latter half of the cycle the fluctuating stress profile evolves as an exact mirror image (with respect to $\sigma = 0$) of the distribution from the first half due to fact that the response is entirely elastic. There is a discontinuity in the curves at the trench ($x/L = 0$) simply because the horizontal stress component σ_{xx} is plotted for $x < 0$ (i.e., in the seafloor) and the dip-parallel component $\sigma_{\xi\xi}$ for $x > 0$ (in the downgoing slab); both stress components are individually continuous. The other noticeable feature is the peaked stress profile near $x = L$. This arises from the relatively abrupt termination of slip which, for the elastic model, essentially acts as the insertion of an edge dislocation of strength $\alpha V_{pl}T_{cyc}/2$ at $t = 0^+$ with a linear decrease to $-\alpha V_{pl}T_{cyc}/2$ at $t = T^-_{cyc}$ (referring to Figure 3). The effective coseismic dislocation at $\xi = L$, Figure 2, compresses material near L in the oceanic plate and dilates material near L above the oceanic plate. The coseismic dislocation also tends to bend the half-space such that material near the fault up dip of L generally rotates clockwise and corresponding material downdip rotates counterclockwise. Both kinds of motion may be more easily visualized by recognizing that the elastic strain field induced by our slip dislocation is the same as that induced by the insertion of a half plane of material under the fault as indicated by the dislocation symbol.

Figure 4b shows the variation of $\sigma_{\xi\xi}$ or σ_{xx} with time during the earthquake cycle at six specific locations along the subducting plate: (1) oceanward, (2) near the trench, (3) under the main thrust zone, (4 and 5) near the lower end of the main thrust zone and (6) beyond. The positions of the corresponding elements for which data were taken for the these plots is shown in Figure 2 and indicated by superposed vertical lines on Figure 4a. Curves are straight, except for jumps at the start of a cycle, because the slip function Δ^{fluct} has a fixed dependence on ξ but varies linearly with time. Curves 1, 2, and 3 have a tensile stress step at $t = 0^+$, followed by a constant rate of compressional stress. Curves 4 and 5 show the opposite response. Curve 6 shows virtually no variation because it coincides with a node in the stress variation for the elastic case (Figure 4a). The extensional stress rate of curves 4 and 5 is attributed, in *Savage's* [1983] discussion of elastic subduction modeling, to steady slip downdip of the main thrust zone during the

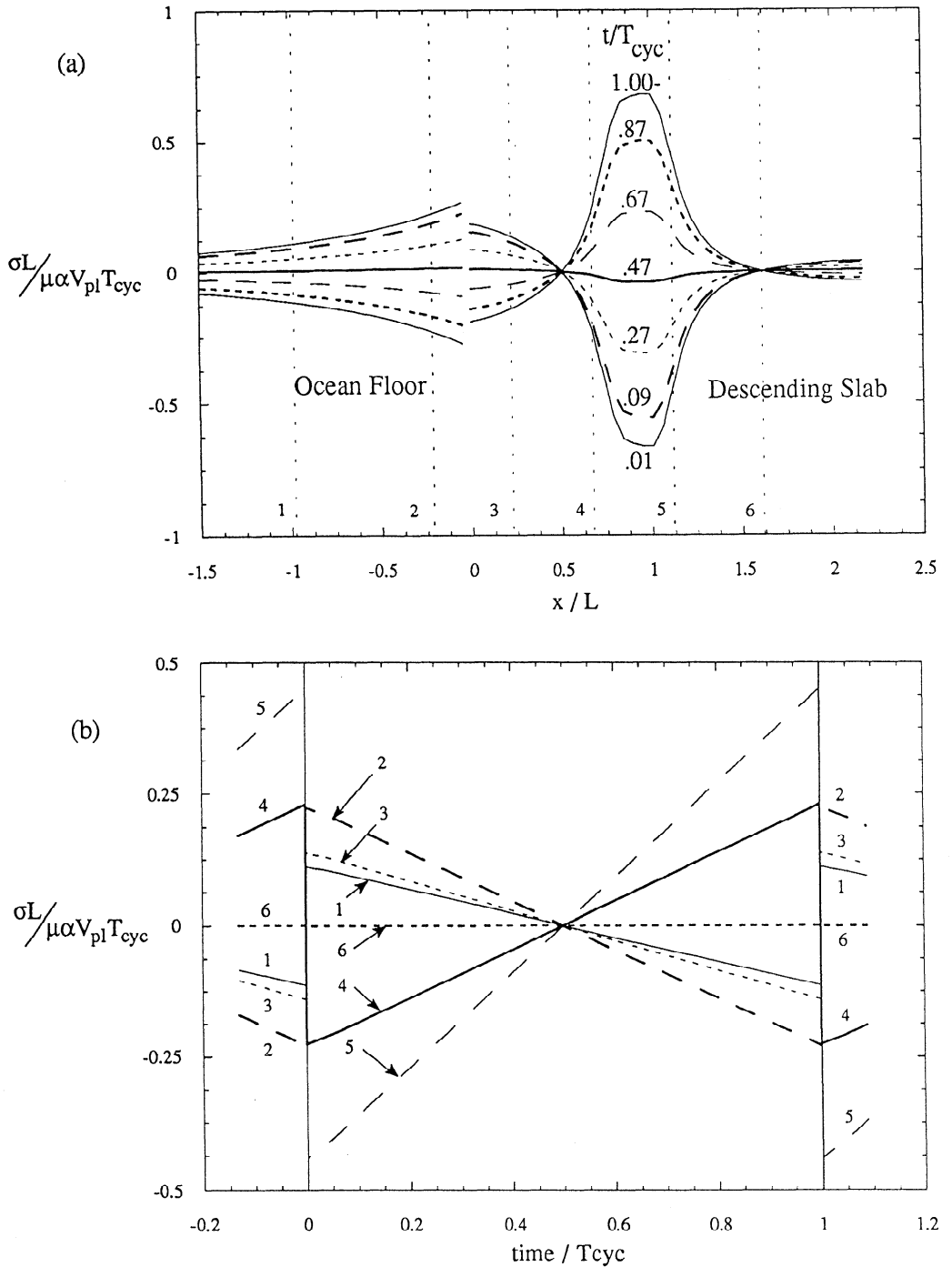

Figure 4. Elastic half-space model. Plots of extensional stress versus (a) distance along fourth element layer of the oceanic plate at successive times t/T_{cyc}, and (b) time for fixed positions of ξ/L, as shown in Figure 2 and Figure 4a.

remaining earthquake cycle; that slip ultimately cancels the coseismic stress pulse and replaces it with a field of opposite sign. Here the intraseismic stress rate has an origin similar to Savage's steady downdip slip but, more generally, is just attributed to the steady average part of the deformation rate field $\dot{u}_i^{avg}(r)$ throughout the subducting region, which is resisted by coupling at the thrust interface. All curves intersect at zero stress halfway through the cycle, because Δ^{fluct} is defined to have zero average over an earthquake cycle. This model, like others to be examined, implies that earthquakes in the subducting plate in the vicinity of the lower end of the main thrust zone would be more likely to have extensional mechanisms late in the earthquake cycle. In the outer rise the opposite but weaker response is expected.

Figures 5a and 5b show how viscoelastic relaxation in the two asthenosphere regions alters the stress field just described for the elastic case. We first present results for the reference case. Figure 5a again shows the variation of extensional stress along the subducting plate at around 13

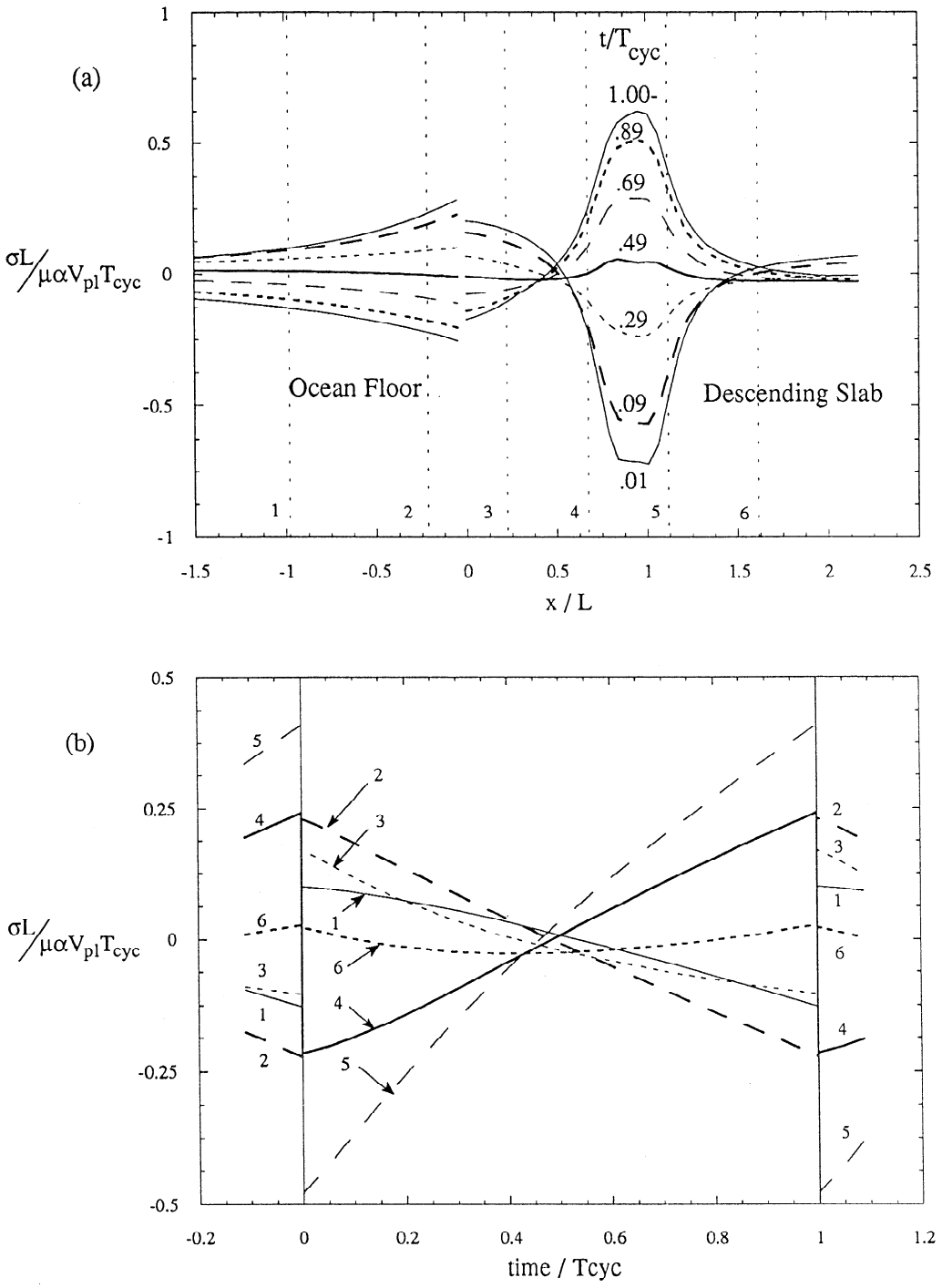

Figure 5. Reference model for T_{rel}/T_{cyc} = 1/6, θ = 25°, and H/L = 3/10. Plots of extensional stress versus (a) distance along fourth layer of the oceanic plate at successive times t/T_{cyc} and (b) time for fixed positions of ξ/L, as shown in Figure 2 and Figure 5a.

km from its surface. Figure 5a is the viscoelastic analog of Figure 4a. It shows, similarly, that at $t = 0^+$, just after mainshock slip, the stress fluctuation in material in a zone with width of the order of L and centered on $\xi = L$ is compressive. Extensional stress fluctuation zones of smaller amplitude lie on both sides of the compressional zone and diminish toward zero at large distance from L. The profile flattens with times increasing toward about t = $0.4T_{cyc}$ and then again evolves to roughly a mirror image of its original shape. In contrast to the elastic case, for which the stress fluctuation reversed sign at $T_{cyc}/2$, the viscoelastic relaxation manifests itself in a reversal of sign earlier in the cycle. The reversal is associated with stress diffusion updip and downdip of $\xi = L$, apparent as a broadening of peaks, both positive and negative. Another indication is that for positions near $\xi = 0.5L$ and $1.5L$ the stress values have the same sign at $t = 0^+$ and T_{cyc}^- as the stress changes back to tensional again, unlike the elastic case where the stress simply changes linearly.

Figure 5b shows the stress-time plots taken from the

sections through Figure 5a as before. At a large distance in the outer rise (curve 1), the tensional stress is almost constant at the beginning of the cycle (and actually rises at positions even further oceanward), before becoming compressional later on. Near the trench, for curves 2 and 3, a compressional rate of $\sigma_{\xi\xi}$ (or σ_{xx}) is maintained throughout the cycle, as in the elastic case, though both curves reach zero stress earlier in the cycle because of an initially higher compressional rate. In curves 4 and 5, for the two points closest to $\xi = L$, the initial extensional rate is even higher than for the elastic case, followed by a diminishing extensional rate. Curve 6 demonstrates the most departure from the elastic case, for which it was essentially nodal. In the viscoelastic case, $\sigma_{\xi\xi}$ initially exhibits a compressional rate of change as that part of the slab absorbs the extension of material near $\xi = L$. However, this is followed by a return to extensional stress late in the cycle as the asthenosphere relaxes.

A simple qualitative explanation of the curves is that at $t = 0^+$ the entire space reacts elastically to the step in Δ^{fluct}. The subducting plate near $\xi = L$ is compressed and the surfaces of the plate temporarily sustain shear stresses which diminish upon relaxation in the adjacent asthenosphere. The relaxation lowers the shear stress on most of the plate surface near $\xi = L$ and allows the subducting plate to locally extend near L, the positive strain $\sigma_{\xi\xi}$ producing an initially positive $\sigma_{\xi\xi}(t)$. The extension in the local relaxed zone is taken up by compression in the downdip part of the oceanic plate. At larger times, around midcycle, the area of relaxed asthenosphere has grown so that relaxation rates are smaller, and the decrease in Δ^{fluct} has canceled the coseismic dislocation at $\xi = L$.

Stress Variation Through Slab Thickness

A plot of $\sigma_{\xi\xi}$ near the top and bottom surface of the ocean plate confirms this explanation. The basic mechanical response is that coseismic slip induces an extensional normal strain $\sigma_{\xi\xi}$, variable over the plate thickness to give slight bending of the plate. Postseismic relaxation and decreasing fluctuating slip tends to undo this. Plate bending shows up on curves as different coseismic values or postseismic rates of $\sigma_{\xi\xi}$ at the top and bottom of the plate. It is easiest to interpret the results by considering point pairs at the same ξ position, one point near the plate top and one near the bottom. The pair of points presented here are located at about ξ/L = 5/4 (locations 5 and 7 in Figure 2).

Figure 6 shows the stress variation for the fourth and eighth (i.e., bottom) element layers of the slab (corresponding to depths of 13 km and 28 km, respectively, from the slab surface for H = 30 km) for both the elastic and the reference viscoelastic models. The responses show coseismic compression of the downgoing slab. The initial postseismic extension rate is greater in the viscoelastic case but subsides due to relaxation as the cycle progresses, with the elastic slab experiencing a greater stress rate late in the cycle. Although the total amplitude of variation is slightly greater in the middle layer of the slab because it is nearer the fault zone, the overall trend shows that there is very little difference in the uniaxial fluctuating stress between the upper and lower sections of the slab below the main thrust zone. Points examined near the trench experience a compressive postseismic stress rate, with concave upward bending followed by compression with increasing distance oceanward. Pairs of points near $\xi = L$ show general concave upward bending during the first half of the cycle and an approximately extensional deformation rate with little bending later in the cycle. The reason for these trends is principally connected to the boundary conditions imposed by the material above and below the slab. Beyond the thrust zone the slab is sandwiched between viscoelastic asthenosphere and the mantle wedge. In our model both have the same relaxation constant T_{rel}/T_{cyc}, and so the slab

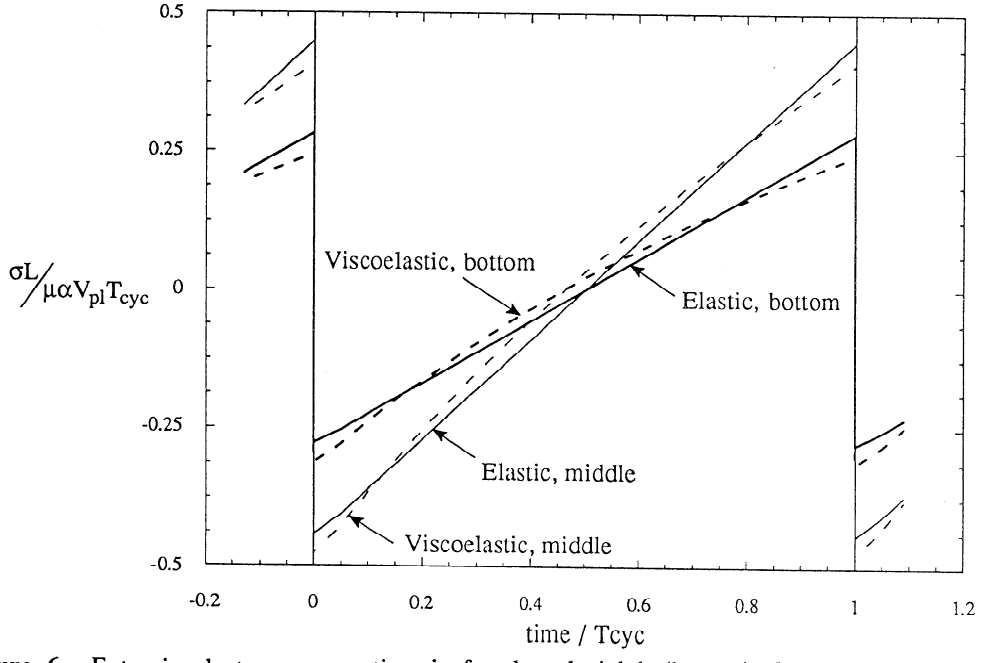

Figure 6. Extensional stress versus time in fourth and eighth (bottom) element layers of subducting plate at $\xi/L \approx 5/4$, for the elastic half-space and viscoelastic reference model ($T_{rel}/T_{cyc} = \infty$ and 1/6, respectively). See positions 5 and 7 in Figure 2.

experiences very similar constraints above and below resulting in the similarity in stress distribution. In reality, it is likely that the mantle wedge would have a shorter Maxwell time [e.g., *Wahr and Wyss*, 1980] than the asthenosphere below the subducting plate. Above the main thrust zone ($\xi < L$) the upper surface of the slab is bound by the locked section of the fault zone in contrast to the viscoelastic asthenosphere on the lower surface. Hence the bottom layer undergoes much higher compression than the upper layer just after the earthquake, before relaxing to support similar magnitude tensional stresses later on in the cycle. These results are broadly consistent with the picture of early expansion of the oceanic plate near L and subsequent upward bending of the plate.

In summary, viscoelastic relaxation modulates the interplay between the seismic stress pulse and its cancellation by steady loading through deep slab and incoming plate motion. Most relaxation occurs near $\xi = L$ during the Maxwell time T_{rel}, expressed here as a fraction of T_{cyc}.

Variation of Model Parameters

We now show the results of varying the model parameters T_{rel}/T_{cyc}, θ, and H, one at a time. Figure 7 shows four plots of the variation of the fluctuating portion of the stress with time, each with one of the parameters varied from the reference case (Figure 5b). When $T_{rel}/T_{cyc} = 1/3$ (Figure 7a), the asthenosphere relaxes more slowly than for $T_{rel}/T_{cyc} = 1/6$, and so the compressional and extensional stress rates (for the regions near the trench and further downdip, respectively) are correspondingly lower, and the stress fluctuation reverses sign slightly later in the cycle. In particular the compressional rates in curves 1 and 3 are sufficiently reduced that curve 3 retains a greater tensional stress for longer, early in the cycle, and sustains a greater compressional stress right to the end of the cycle, in contrast to the reference case where the increased compressional rates cause the curves to cross once again before the next event. Conversely, when $T_{rel}/T_{cyc} = 1/12$ (Figure 7b), the stress rates are higher and the stress reverses earlier in the cycle. The pattern of curves 1 and 3 is the same as that for the reference case though more accentuated. During the second half of the cycle there is less discrepancy in the stress rates.

For an angle of subduction of 20° (not shown here) the magnitudes of the initial postseismic stress rates are again lower than in the reference case, and stress reversal occurs later. In particular, the compressional rate in curve 1 is greatly reduced compared to the other curves due to the less extreme change in angle of the slab at the trench. Increasing the angle of subduction to 30° (Figure 7c) has the opposite effect of increasing the stress rates and inducing an earlier reversal of stress. In this sense, decreasing the angle of dip in a viscoelastic model causes similar trends in midplate extensional stress histories in the subducting plate, as does increasing the inherent Maxwell time of the asthenosphere. However, our results show that stress histories in the bottom layer of the slab at around $\xi/L = 5/4$ (position 7 in Figure 2) are relatively insensitive to dip angle.

Increasing the thickness of the slab, even to $H = L/2$ (Figure 7d), has little effect (as also found by *Melosh and Raefsky* [1983]), and although the stress rates and magnitude of the stresses are moderately reduced, the trends are almost the same as for the reference case. One slight variation is that curve 1 for the far outer rise region decreases monotonically for the thicker slab, so attaining a lower compressional stress at the end of the cycle than curve 3, as with the longer Maxwell times and smaller angles of dip.

Stress and Seismicity in the Seafloor Toward the Outer Rise

In order to relate the stress changes from our model with those that occur in regions of subduction, our results can be compared with those implied from fault plane solutions of oceanic intraplate earthquakes. The main observational constraints on the total stress field in the oceanic plate are summarized on the worldwide composite plot of *Lay et al.* [1989], Figure 8. The left side shows that late in the cycle, before the next main thrust event, earthquakes in the ocean floor between the trench and the outer rise (referred to as "outer rise events") are almost entirely compressional. After the main event the pattern is the opposite. In the global data set the overall number of the well-known extensional outerrise earthquakes greatly exceeds the number of compressional earthquakes before (some zones have no compressional events before, some others may have no extensional events afterward). This plot implies that the principal stress driving seismicity, whether compressive or tensile, is aligned with the direction of plate motion. The plot also implies that the stress fluctuation fields before and after the main event are somewhat homogeneous, otherwise there would be a mixture of earthquake mechanisms in each time interval. The right side of Figure 8 shows that at intermediate depths compressive earthquakes become more frequent after the main thrust zone event. Tensional events become less frequent, at least during the first few years. The stress field is apparently less homogeneous than for the outer rise, since both kinds of earthquakes occur before and after the main event.

The data summarized in Figure 8 forces us to accept that the stress fluctuations associated with the great earthquake cycle cause observable effects, even at the distances of these events which are up to nearly 100 km or so from the main rupture zone. However, our calculations suggest that the cycle-related extensional stress fluctuations at such locations in the outer rise range over only 0.1 to 0.5 MPa (1 to 5 bars); this is found by taking $\alpha V_{pl} T_{cyc} = 1$ to 3 m, $L = 100$ km, and $\mu = 30$ GPa and noting dimensionless fluctuations from Figures 4 and 5.

Figure 9, modified from *Dmowska and Lovison* [1988], shows how these modest stress fluctuations may induce and suppress seismicity. Because of active bending in the outer rise, the local stresses in the ocean plate should be near a condition for extensional normal faulting at shallow depths, or in some cases near a condition for compressional failure at greater depth, or for both. The dashed lines show the condition for extensional or compressional failure, and the solid lines represent the proposed variation of the average stress with depth. Thus the superposition of the small stress changes of the earthquake cycle may be enough to tip the balance. The fluctuating trench-perpendicular component of stress becomes extensional just after the thrust event and thus favors extensional faulting in the outer rise, but it

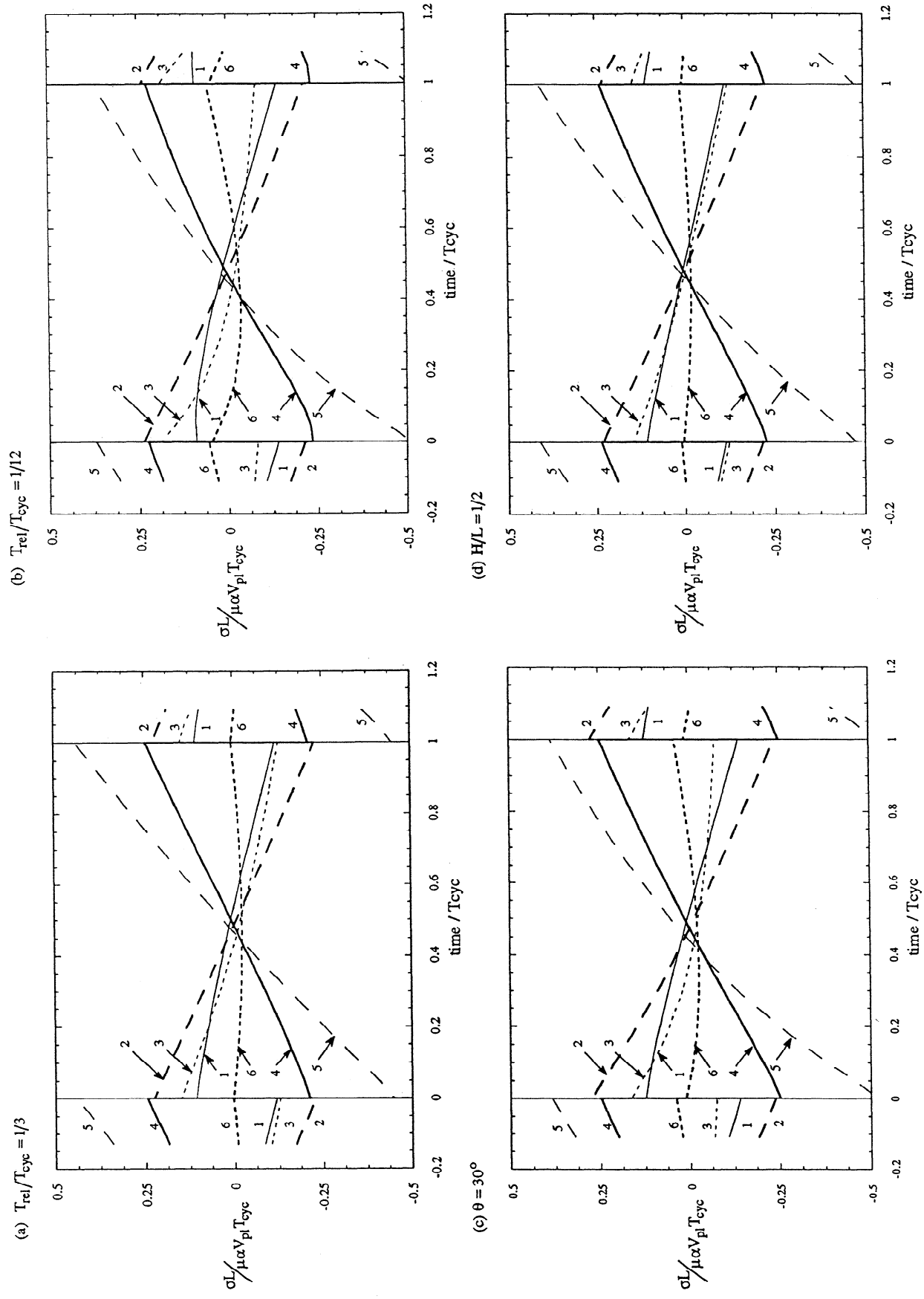

Figure 7. Extensional stress versus time for varying parameter cases: (a) $T_{rel}/T_{cyc} = 1/3$, $\theta = 25°$, and $H/L = 3/10$, (b) $T_{rel}/T_{cyc} = 1/12$, $\theta = 25°$, and $H/L = 3/10$, (c) $T_{rel}/T_{cyc} = 1/6$, $\theta = 30°$, and $H/L = 3/10$, (d) $T_{rel}/T_{cyc} = 1/6$, $\theta = 25°$, and $H/L = 1/2$.

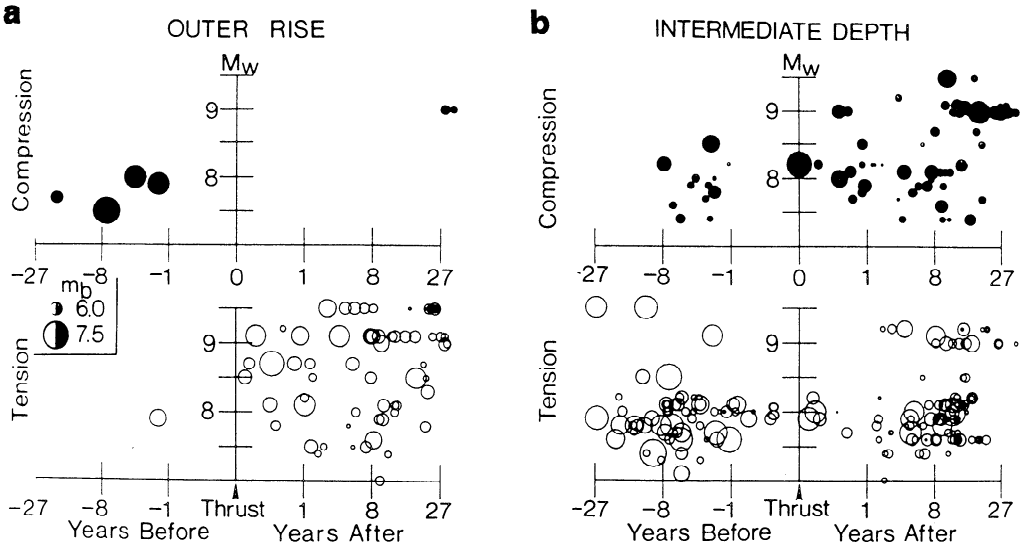

Figure 8. Composite plots of (a) outer rise and (b) intermediate depth earthquakes within the oceanic plate. Earthquake times are shown relative to the time of a large or great thrust event on the adjacent interface, and the moment magnitude of that event is plotted on the vertical axis. Solid symbols are for compressional events, and open symbols are for extensional; symbol sizes scale with earthquake magnitudes, from *Lay et al.* [1989].

gradually diminishes and turns toward compression. The extensional outer rise activity is then suppressed, and, in some places, compressional outer rise events are induced. The basic trends in stress from tensional to compressional in the outer rise are exhibited by our model. In particular, curve 1 in Figure 5b shows how tension may be sustained (or increase) during the initial period after the main event and so induce tensional earthquakes in that region during this period. Although the majority of outer rise earthquakes occur between 25 and 75 km ($-3/4 \leq x/L \leq -1/4$) from the trench and point 1 lies around $x/L = -1$, it nevertheless demonstrates the way in which relaxation of the asthenosphere can lead to stress fluctuations not predicted by a simply elastic model.

Effect of Shallow Aseismic Portion of Thrust Interface

It is reasonable to assume that a region should remain seismically active while the stress motivating seismicity is large and increasing, but not when it is decreasing. This poses a problem for our model because the shape of curves for σ_{xx} in Figures 4, 5, and 7 for the outerrise locations, 1 and 2, suggest that in most of the region where seismicity occurs, σ_{xx} is large but decreasing. Recent work by *Dmowska et al.* [1994] shows, however, that this feature is an artifact of our seismically slipping the entire thrust interface in the model up to the trench. They show that when the top of the seismically slipped zone does not extend all the way

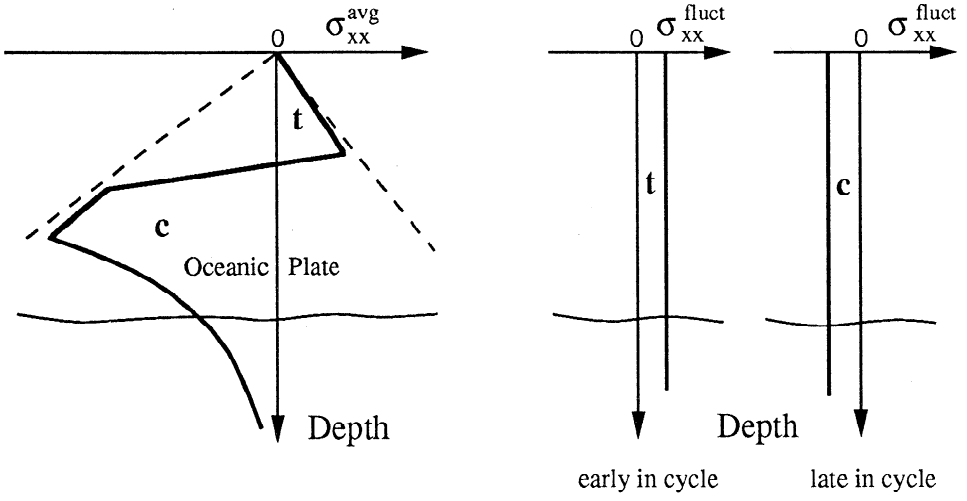

Figure 9. Average stress state in the outer rise and superposed effect of stress fluctuations, tensional *t* early in the cycle and compressional *c* later in the cycle; modified from Dmowska and Lovison (1988).

to the trench, and when an aseismic viscous rheological behavior is assumed on the interplate interface between the trench and the top of the zone, then histories of σ_{xx} at representative locations of outer rise earthquakes show an increase at the time of the great earthquake, but then a continuing increase as that aseismic zone relaxes, and finally decreasing as the cycle matures.

In order to investigate this effect in the model presented here, an aseismic zone of length L' was assigned to the shallow portion of the fault zone between the trench and the top of the thrust interface in the model. The length L' is marked in Figure 2 and was chosen so as to extend to a sufficient depth underneath the overriding plate, in this case around 16 km for L = 100 km, that is, $L'/L \approx 0.37$. The material in the aseismic zone is Maxwell viscoelastic with shear modulus μ_f, Poisson's ratio ν_f, and viscosity η_f. For a long thin viscous zone ($L' >> h$, the width of the fault), the relevant viscosity parameter is η_f/h such that the relative slip of one side of the fault to the other per unit applied shear stress is h/η_f. The effective system relaxation time $T_{\text{rel}}^{\text{sys}}$ for such a fault can be extracted from the treatment of a thin inclusion by *Rice* [1980]:

$$T_{\text{rel}}^{\text{sys}} = \frac{\eta_f}{\mu_f} + \frac{qL'\eta_f}{\mu h} \tag{4}$$

where q is a factor of order unity. In our model the shear and bulk moduli are the same as in the mantle, so $\mu_f = \mu$ and (4) reduces to

$$T_{\text{rel}}^{\text{sys}} = \frac{\eta_f}{\mu h}(h + qL') \tag{5}$$

In order to see the effect of relative relaxation time of the aseismic zone compared to the mantle on the stress history in the outer rise, the model was run with varying values of η_f (and hence varying values of $T_{\text{rel}}^{\text{sys}}$) and these are referenced here by expressing the relaxation time of the aseismic zone system as a fraction of the earthquake cycle $T_{\text{rel}}^{\text{sys}}/T_{\text{cyc}}$. The resulting fluctuating portion of the stress in the outer rise at positions 1 and 2 (see Figure 2) against time is presented in Figure 10 for values of $T_{\text{rel}}^{\text{sys}}/T_{\text{cyc}}$ of ∞, 1/4, 1/8, 1/16, 1/32 and 0, the first and last representing the limit cases of a purely elastic aseismic zone and an aseismic zone with free slip respectively. Note that the stress is nondimensionalized with respect to L' not L, as that is the relevant length scale here. Figure 10a shows the variation of stress at position 1, and Figure 10b shows the variation of stress for position 2. For values of $T_{\text{rel}}^{\text{sys}}/T_{\text{cyc}}$ greater than about 1/2 there was very little difference in response of the fluctuating stress from the infinite case. By comparing these with the stress fluctuation for those same positions with the coupled zone extending right up to the trench in Figure 5b, it is apparent that there are two principal changes introduced by the aseismic zone. The first is that the magnitude of the fluctuations is smaller by a factor of about 3 in the outer rise as the tensional and compressional stresses induced by the imposed slip of the coupled zone are dampened by the viscoelastic aseismic length of the fault. The second, more striking difference, is that stress becomes significantly more tensional after the main event before once again subsiding to compressional. The stress reaches a maximum sooner after the main event with increasing distance from the trench as the effects of the aseismic zone decrease farther from the trench, and the amplitude of fluctuation is less at position 1, farther from the trench, than position 2 as before. As $T_{\text{rel}}^{\text{sys}}/T_{\text{cyc}}$ decreases, the stress fluctuations increase and the stress becomes compressional earlier as the curves approach the limit of $T_{\text{rel}}^{\text{sys}}/T_{\text{cyc}} = 0$, where the stress decreases monotonically through the cycle. These findings are consistent with those of *Dmowska et al.* [1994].

Figure 10 can be used to relate times for the continued increase in tension (and hence seismicity) toward the outer rise to the corresponding values of $\eta_f/\mu h$ for typical model parameters. Selecting values to fit the geometry of the reference model, we consider a 25° dipping slab of 30 km thickness and a thrust zone of length L = 100 km, of which the shallowest 37 km (L') is aseismic with an asthenosphere in which the Maxwell time $T_{\text{rel}} = T_{\text{cyc}}/6$. Examining Figure 10b, which refers to a location which is then 21 km toward the outer rise from the trench, for a recurrence time of 100 years the curves for $T_{\text{rel}}^{\text{sys}}/T_{\text{cyc}}$ = 1/32 and 1/16 imply that the fluctuating extensional stress will continue to increase in tension for 19 years if $\eta_f/\mu h$ = 0.11 yr km^{-1} and for 29 years if $\eta_f/\mu h$ = 0.22 yr km^{-1}. If the recurrence time is halved to 50 years, increases in tension will occur for 9.5 years if $\eta_f/\mu h$ = 0.05 yr km^{-1} and for 14.5 years if $\eta_f/\mu h$ = 0.11 yr km^{-1}.

With or without the incorporation of an aseismic zone in the model, stress fluctuations from both outer rise curves (positions 1 and 2) eventually become compressional later on in the cycle in accordance with the observed events preceding the next thrust event. Since compressional outer rise events signal the maturity of a locked gap, they are important intermediate term precursors [*Dmowska and Lovison*, 1988], but they do not always occur, suggesting that it is less usual for the stress deep in the plate to be near to the failure threshold as in Figure 9.

Stress and Seismicity in the Slab at Intermediate Depth

At intermediate depth the trends are less clear from Figure 8, but directly after the main event there is a gap in tensional activity, while compressional events occur with greater frequency. This is consistent with the fact that postseismic stress fluctuations are initially compressional at depth in the slab (curves 4 and 5 in Figure 5b) and, in particular, with the manner in which curve 6 has an initial compressional rate before returning to tension in the late cycle.

In general, in the outer rise, the slab at intermediate depths and in the back arc regions of the overlying plate, we expect representative values of the time-averaged stresses σ_{ij}^{avg} to be much larger than the fluctuations $\sigma_{ij}^{\text{fluct}}$. Thus the type of seismicity produced in a particular location is determined by σ_{ij}^{avg} and, indeed, that type of seismicity is our most important way of characterizing the principal directions of σ_{ij}^{avg}. However, it is the modulation of σ_{ij}^{avg} by the small but time dependent perturbations $\sigma_{ij}^{\text{fluct}}$ that we have estimated and plotted here, which turns that seismicity on or off. We suspect that σ_{ij}^{avg} is of relatively simple form in the outer rise, somewhat like that indicated on the left in

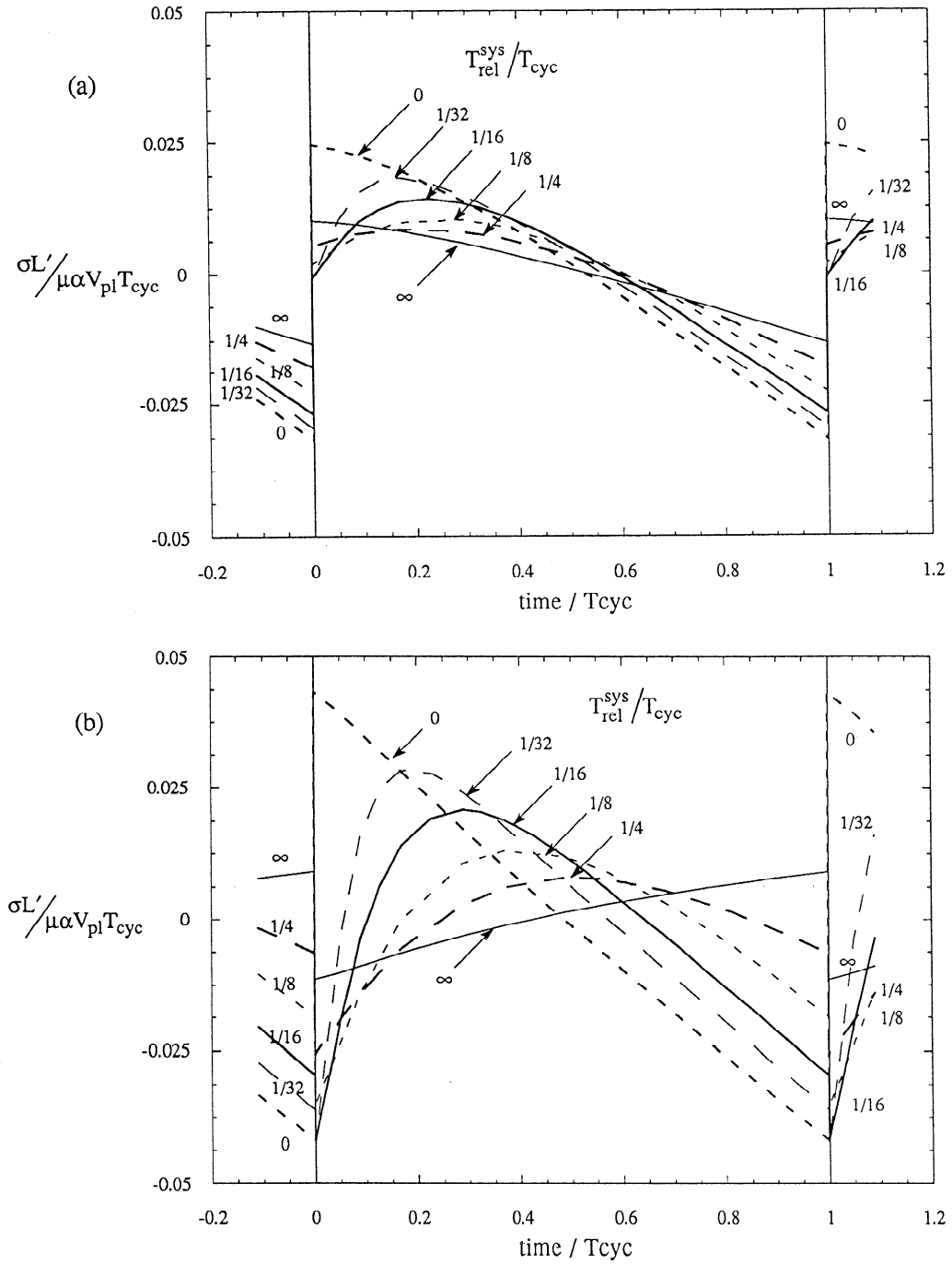

Figure 10. Reference model for T_{rel}/T_{cyc} = 1/6, θ = 25°, and H/L = 3/10 with an aseismic zone of length 0.37L incorporated in the fault zone. Extensional stress versus time for different values of T_{rel}^{sys}/T_{cyc}, (a) for position 1 and (b) position 2 in Figure 2.

Figure 9 and with horizontal and vertical principal directions. Also, we find that σ_{ij}^{fluct} amounts to essentially a horizontal stress σ_{xx}^{fluct} with little thickness variation, much like that shown on the right in Figure 9. These features result in the clear time-in-cycle dependence of outer rise seismicity, as shown by the data in Figure 8. In contrast, the slab at intermediate depth may have a more complex average stress field, possibly influenced by thermal stressing, dehydration and unbending. Also, the fluctuations σ_{ij}^{fluct} there are not limited to essentially a single component of stress. Thus while the same principle, that seismicity of type determined by σ_{ij}^{avg} is modulated by σ_{ij}^{fluct}, should apply at intermediate depth, the resulting time dependence of seismicity is not as simple as for the outer rise.

Surface Deformation of the Continental Plate

Figure 11a shows the variation of the fluctuating part of the extensional strain (normal to the trench) ε on the Earth's surface with distance from the trench for the reference model. Curves are plotted for various times during the earthquake cycle. The general trend is that strain changes from positive to negative in peaks either side of the position

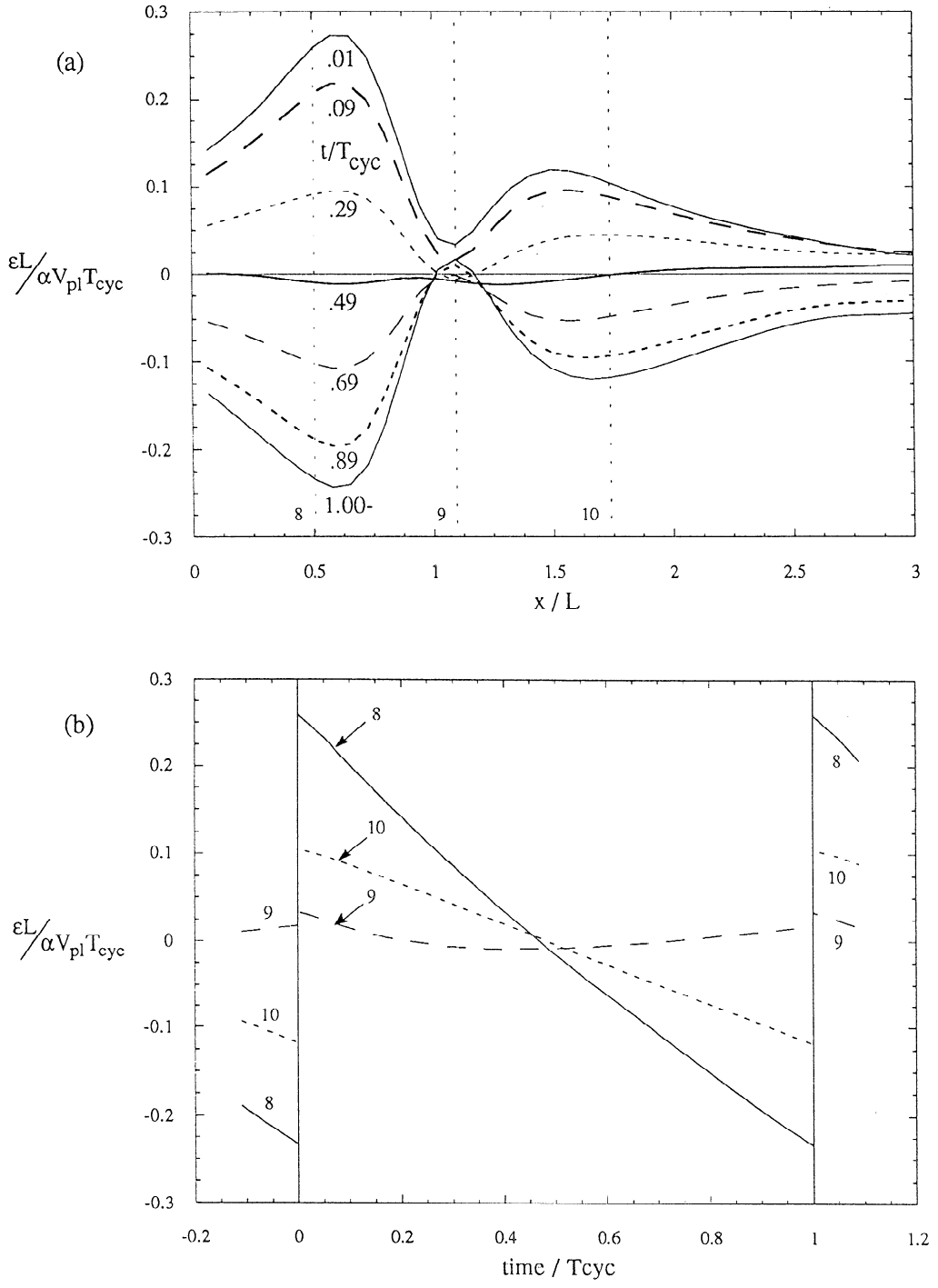

Figure 11. Reference model for plots of extensional surface strain versus (a) distance along the continent surface at successive times t/T_{cyc} and (b) time for fixed positions of x/L, as shown in Figure 2.

above the locked zone in the slab during the cycle. The strain diminishes to around zero at this region. The plot of strain for the purely elastic case exhibits similar symmetry as for variation of stress in the slab. For that case the strain response in the second half of the cycle grows to an exact mirror image of that in the first half with respect to $\varepsilon = 0$ with a node at $x/L = 1$. However, the effects of the viscoelastic relaxation destroy this symmetry, as can be seen in Figures 11a and 11b. Figure 11b shows the variation of ε with time at three specific points along the surface as indicated by the numbers in Figure 2 and the lines on Figure 11a. For positions at distances around L/2 in front of or beyond the projection of the downdip end of the locked zone onto the surface of the overriding plate, the strain rate is continuously compressional during the cycle (curves 8 and 10), although the strain is less in magnitude everywhere beyond the end of the locked zone. However, above the downdip end of the locked zone the strain rate is

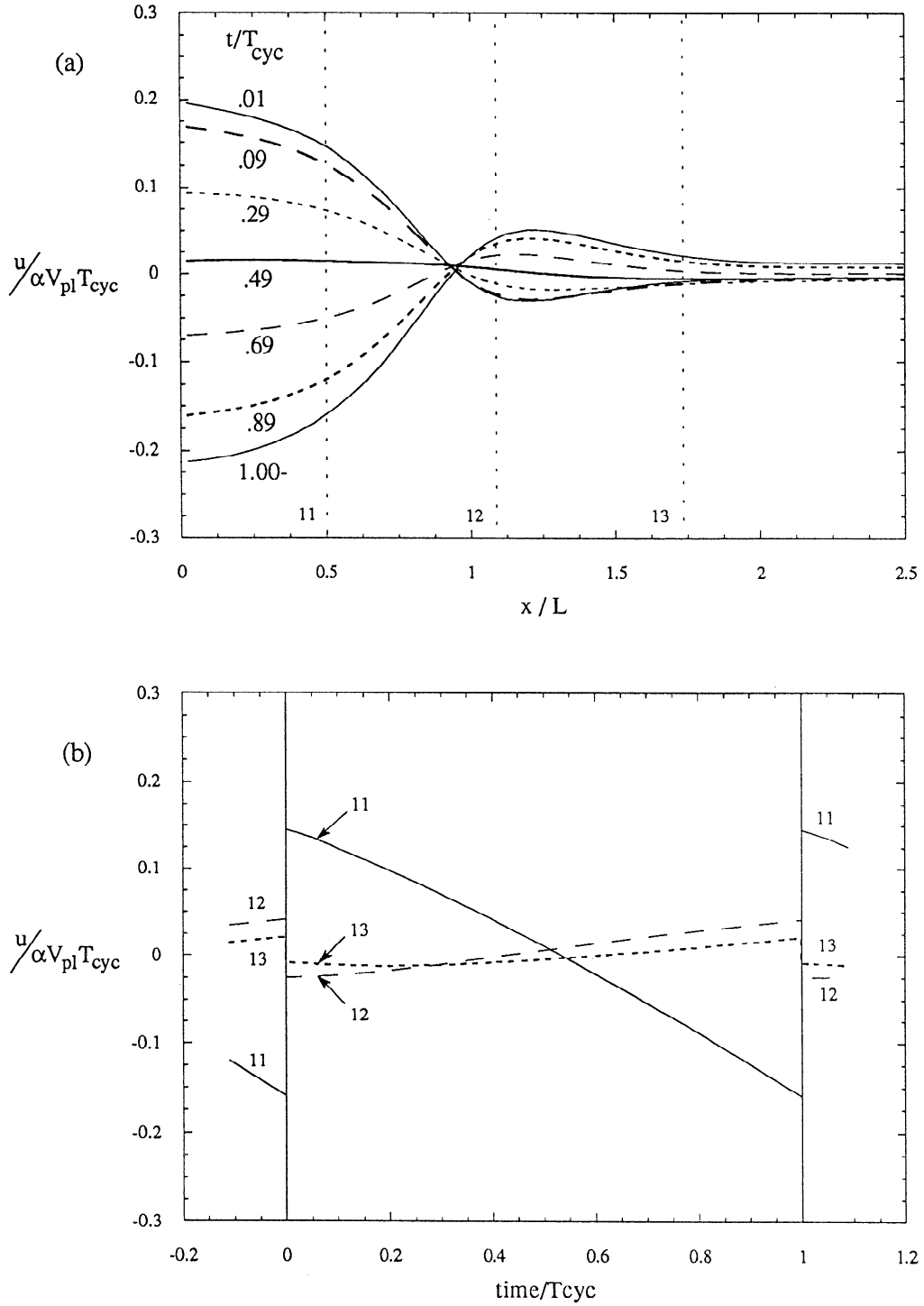

Figure 12. Reference model for plots of vertical surface displacement versus (a) distance along the continent surface at successive times t/T_{cyc} and (b) time for fixed positions of x/L, as shown in Figure 2.

initially compressional but then changes to extensional during the first half of the cycle and causes the strain rate to become positive once more in the latter half. This is an effect of viscoelastic relaxation in the mantle wedge, as first noted by *Rice and Stuart* [1989].

Figures 12a and 12b show a similar analysis for the vertical displacement u (positive for uplift) along the continent surface in the reference case model. Figure 12a shows the variation of displacement with distance from the trench for increasing times during the cycle and Figure 12b shows the "history" plots at the same regions along the surface as in Figure 11a. Note that displacement data is taken from nodes in the finite element mesh in contrast to the stress and strain data which is extracted from the position of the element centroids hence the positions of points 11-13 are slightly different from 8-10 as shown in Figure 2. In Figure 12a the general trend is change in displacement from uplift to subsidence for positions on the

overriding continental plate above the locked zone (i.e., for $x/L \leq 1$) and changes in the opposite sense beyond this zone. The elastic case again shows exact symmetry with respect to $u = 0$ during the cycle in contrast to the viscoelastic model. The history plots in Figure 12b show that above the locked zone (curve 11) the displacement rates shows subsidence throughout the cycle, whereas beyond it, displacements start initially negative with subsidence but are rapidly converted into uplift the nearer the point is to the locked zone. Both the subsidence and uplift rates increase during the cycle in contrast to the elastic case where they remain constant throughout. We note that it would be difficult to infer the mantle Maxwell time ($T_{cyc}/6$ in the case shown) from the shape of these uplift curves.

Previous two dimensional finite element modeling of subduction zones by *Rice and Stuart* [1989] incorporating a viscoelastic mantle wedge of relatively short relaxation time found an area of late-cycle extensional straining on the Earth's surface, above the downdip end of the locked zone, where compressional straining dominated in a purely elastic model. Subsequently, *Zheng et al.* [this issue] have specifically modeled the Shumagin Islands region, Alaska, positioning the dipping slab interface from seismicity locations in that region and choosing parameters such as T_{rel}/T_{cyc} and α (as used in this work) to fit the surface strain, uplift, and tilt data with that predicted by their model. They conclude that the observed deformation data can be fit by models for which the interface is coupled with $\alpha \approx 0.15$ to 0.20; such a degree of coupling is consistent with repeats of events like the $M_S = 7.4$ earthquake of May 31, 1917, in that region over 50 to 100 year recurrence intervals. However, to fit the data, they find that models must have relaxation times in the mantle wedge or along the slab surface downdip of the coupled zone that are small fractions of the recurrence interval.

The more generic subduction model presented here does not attempt to fit all the parameters of any specific region and so ignores such features as the change of dip angle in the subducting slab with depth and a locked zone that does not reach all the way to the trench. However, comparison of the resulting fluctuating fields from our model with those of *Zheng et al.* [this issue] shows that the broad trends in surface strain and uplift are maintained. In particular, the change from compressional to extensional strain later on in the cycle above the downdip end of the locked zone is observed (see curve 9 in Figure 11b) compared to simply a compressional strain rate throughout the cycle further downdip or toward the trench. The vertical displacement data also show the same decreasing trend throughout the cycle trenchward of the end of the locked zone and reversion to uplift from subsidence above and beyond the locked zone later in the cycle.

We do not further discuss here the variation of uplift and strain with model parameters θ, T_{rel}/T_{cyc}, H, etc. The experience by *Zheng et al.* [this issue] shows that such predictions are very strongly controlled by the geometrical position of the thrust interface, including its curvature and variation of locking along it, and both variations have been ignored in our generic modeling here.

Other subduction zones that have been studied, specifically in regard to surface deformation of the overriding plate, include the Cascadia subduction zone, northwestern America and the Nankai subduction zone, southwestern Japan. Attempts have been made to fit surface strain and uplift data from these areas with both elastic half-space models and models incorporating regions with viscoelastic properties.

Savage et al. [1991] examined strain accumulation from their Olympic and Seattle trilateration networks in western Washington [*Savage et al.*, 1991, Figures 4 and 7] and compared data with predictions of a two-dimensional elastic half-space model with 10° dip and a locked zone of width around 100 km. The cycle time of this region is estimated to be of the order of 600 years. They found that there is rough agreement between the interseismic deformation rate predicted by a fully locked ($\alpha = 1$) elastic model and that actually observed. However, measuring along a line perpendicular to the trench, both networks lie over 200 km away, which corresponds to a position beyond point 10 in our plot, Figure 11a, of fluctuating extensional strain with distance along the continent surface. Although the amplitude of fluctuation decreases slightly with increasing distance from the trench away from point 10, the change with time remains very similar. From Figure 11b this change can be seen to be a virtually linear decrease with time, that is, to give essentially the same strain rate as would be predicted by a purely elastic model. So this shows that a viscoelastic model with Maxwell time much shorter than the recurrence interval is also consistent with strain data at such locations and, in fact, the strain response there is largely insensitive to mantle relaxation.

Savage [1995] also examined uplift deformation at the Nankai subduction zone, where the recurrence interval is about 100 years. Good sea level records are available from 15 tide gauges in the area around the subduction zone for the period 1951-1990, which corresponds to most of the first half of the current interseismic interval. The data is grouped into uplift at three "profiles", western, central and eastern, which correspond to three lines of gauges running roughly perpendicular from the trench [*Savage*, 1995, Figure 1]. Savage compares the uplift data with predictions from an elastic half space model and the viscoelastic model of *Thatcher and Rundle* [1984a,b] of an elastic plate over a viscoelastic half space, and finds that although neither model provides a good quantitative fit to the data, both models furnish a qualitative explanation for observed uplift rates. Savage concludes accordingly that it is difficult to demonstrate the need for viscoelastic relaxation of the asthenosphere, in addition to what he attributes to a rapid postseismic extension of slip into the downdip continuation of the coupled zone with relaxation time of about 5 years. Comparison with two dimensional (2-D) model results is complicated by the fact that the proposed area of rupture (and hence coupled zone) varies considerably along strike, both in width and in distance between the top of the locked zone and the trench. The eastern profile lies over the middle section of the rupture where the coupled zone is about 95 km in width and extends almost to the trench, and that profile seems most suitable for comparison to 2-D models. The central profile similarly lies over the middle section of the rupture, but the width of the coupled zone seems to extend significantly further downdip in its vicinity, introducing three dimensional (3-D) effects unaccounted for in the model, and the the western profile is at the far western end of the rupture zone where 3-D end effects would be dominant. For the eastern profile the first station lies at a position

corresponding to a point just beyond point 11 in Figure 12a and exhibits a decreasing uplift rate in the first half of the cycle. The other stations lie between points 12 and 13 in Figure 12a and show an increasing uplift rate during that period. A fit to the uplift data with quadratic variation in time is provided by *Savage* [1995, Table 2], after removing the effect of the rapid postseismic transient, and confirms that the uplift rates change from decreasing uplift rate to increasing uplift rate with time as the station positions move farther from the trench. The same trend is predicted in Figure 12b and is a result of the viscoelastic relaxation in the mantle; had such not been included, the uplift rates would be uniform in time. Still, for the station corresponding to point 11 the observed uplift rate diminishes from a positive value around 1960 to nearly zero around 1990, rather than being negative throughout the interval as in Figure 12. The central profile shows, for the station closest to the trench and roughly corresponding to point 11 in Figure 12a, the predicted increasingly negative uplift rate with time, but the remaining stations of that profile, and the entire western profile, do not show the predicted systematic variation of rate of change of uplift rates with distance from the trench.

The main variation in the fluctuating surface strain with time compared to the elastic case occurs in a region above and slightly inland from the end of the locked zone. The plots in Figures 11 and 12 are for T_{rel}/T_{cyc} = 1/6, but even for T_{rel}/T_{cyc} = 1/12, where the Maxwell time is an order of magnitude smaller than the cycle time, the variations in surface strain and uplift rates away from this region are very small. We have found the results of our simplified viscoelastic model to be consistent with the data presented by *Savage et al.* [1991] and *Savage* [1995], although the viscoelastic relaxation does not have very large effects on the regions or type of data examined there.

Conclusions

In this work we have used the finite element method to analyze a generic 2-D model of a coupled subduction zone. The model is simplified to have a fixed dip angle and fixed plate thicknesses. A complete description of the total stress and displacement rate fields comprises a superposition of long term average fields and fluctuating portions. Periodic slips in the underthrusting events correspond to imposition of a sawtooth time history of slip along the interface which drives the fluctuating part of the fields that we calculate.

The resulting variations in stress fluctuations in space and time are generally consistent with observed dependence of seismicity and earthquake mechanisms on time in the subduction cycle. These observations show trench-normal extensional earthquakes occurring early in the cycle in the outer rise. They occur most abundantly in the later portions of the cycle in the subducting slab below the main thrust zone. Compressional earthquakes have the opposite behavior; the rare ones occurring in the outer rise are late-cycle phenomena, so much so that they mark the maturity of the earthquake cycle, and they are most likely in the slab at intermediate depth in the period shortly following the thrust event.

We assume that the overlying and subducting plates respond elastically to the stress fluctuations of the earthquake cycle. When the mantle regions also respond elastically, the stress and displacement rates at each point are uniform throughout the intraseismic period. Viscoelastic mantle response changes this feature, with reversal of the sense of the stress fluctuation occurring earlier in the cycle, but additional complexity exists due to stress diffusion in the slab.

The stress fluctuations that we calculate in the outer rise and descending slab are relatively small, yet observations show that the timing of seismicity does correlate with those fluctuations. We believe that such seismicity occurs in locations where the time-averaged stresses (e.g., corresponding to a bending field in the outer rise) are large and near to a failure condition. The role of the small but time-dependent fluctuations of stress is to modulate those average stresses, moving the total stress toward or away from failure and thus controlling the timing of seismicity.

Variation of the model parameters demonstrates that an increase in the viscoelastic relaxation time of the mantle or in slab thickness, or a decrease in dip angle, produce similar responses in the midplate stress histories in the subducting seafloor. There is a reduction in initial strain rate magnitudes, and the reversal in stress fluctuations occurs later in the cycle.

The introduction of an aseismically slipping zone at the trench end of the thrust interface, with viscous response properties, modifies the time history of the stress fluctuation in the seafloor toward the outer rise in a way that seems critical to explaining the extended time period over which shallow extensional outer rise events occur after a major underthrust. When the coupled zone extends directly to the trench, the stress in the outer rise is increased in extension by the underthrust but then diminishes with continuing time throughout the earthquake cycle, which is inconsistent with the extended period of observed seismicity. When a shallow aseismic part of the thrust interface is included in the model and given suitable viscous properties, it is found instead that the stress in the outer rise in locations where such earthquakes commonly occur continues to increase in extension throughout the early part of the cycle. Estimates of the duration of this increase have been related to model parameters.

When the mantle responds elastically, strain rates along the Earth's surface show compression at a uniform rate throughout the intraseismic period. However, an important effect of viscoelastic relaxation in the mantle, and especially in the mantle wedge, is that the surface strain rate in a region located above and slightly inland from the downdip end of the coupled region changes from compressional early in the cycle to slightly extensional as the cycle matures. Such an effect has helped to rationalize the observed lack of significant strain accumulation in the Shumagin Islands, Alaska, geodetic network, so that the lack of compressional strain need not signify the lack of significant coupling [*Zheng et al.*, this issue]. Apart from these effects on surface straining, our modeling shows that even the assumption of rapid mantle relaxation, for example, with Maxwell time an order of magnitude smaller than the recurrence interval, causes only modest time variation in intraseismic uplift rates along the surface of the overriding plate and extensional stress rates along the subducting plate.

Acknowledgments. This work has been supported at Harvard by the USGS through NEHRP grants 1434-93-G-2276 and 1434-94-G-2450. The work originated in a collaboration by J. R. Rice and W. D. Stuart in 1988-1989 and included support at that time from a Fairchild Fellowship for J. R. Rice at Caltech and from the NSF Division of Earth Sciences program. We are grateful for review comments by S. C. Cohen, J. C. Savage, N. H. Sleep, W. Thatcher, and an anonymous reviewer.

References

Astiz, L., and H. Kanamori, Interplate coupling and temporal variation of mechanisms of intermediate-depth earthquakes in Chile, *Bull. Seismol. Soc. Am., 76*, 1614-1622, 1986.

Astiz, L., T. Lay, and H. Kanamori, Large intermediate-depth earthquakes and the subduction process, *Phys. Earth Planet. Inter., 53*, 80-166, 1988.

Christensen, D. H., and L. J. Ruff, Outer-rise earthquakes and seismic coupling, *Geophys. Res. Lett., 10*, 697-700, 1983.

Christensen, D. H., and L. J. Ruff, Rupture process of the March 3, 1985 Chile earthquake, *Geophys. Res. Lett., 13*, 721-724, 1986.

Christensen, D. H., and L. J. Ruff, Seismic coupling and outer rise earthquakes, *J. Geophys. Res., 93*, 13,421-13,444, 1988.

Cohen, S. C., Evaluation of the importance of model features for cyclic deformation due to dip-slip faulting, *Geophys. J. Int., 119*, 831-841, 1994.

Dmowska, R., and L. C. Lovison, Intermediate-term seismic precursors for some coupled subduction zones, *Pure Appl. Geophys., 126*, 643-664, 1988.

Dmowska, R., and L. C. Lovison, Influence of asperities along subduction interfaces on the stressing and seismicity of adjacent areas, *Tectonophysics, 211*, 23-43, 1992.

Dmowska, R., J. R. Rice, L. Lovison, and D. Josell, Stress transfer and seismic phenomena in coupled subduction zones during the earthquake cycle, *J. Geophys. Res., 93*, 7869-7884, 1988.

Dmowska, R., G. Zheng, and J. R. Rice, Rheological and tectonic controls on stressing history and seismicity in the outer-rise during the earthquake cycle: Oaxaca 1978, Mexico, segment (abstract), *Eos, Trans, AGU, 75* (44), Fall Meet. Suppl., 449, 1994.

Dmowska, R., G. Zheng, and J. R. Rice, Seismicity and deformation at convergent margins due to heterogeneous coupling, *J. Geophys. Res.*, in press, 1996.

Jarrard, R., Relations among subduction parameters, *Rev. Geophys., 24*, 217-284, 1986.

Kanamori, H., Great earthquakes at island arcs and the lithosphere, *Tectonophysics, 12*, 187-198, 1971.

Lay, T., L. Astiz, H. Kanamori, and D. H. Christensen, Temporal variation of large intraplate earthquakes in coupled subduction zones, *Phys. Earth Planet. Inter., 54*, 258-312, 1989.

Melosh, H. J., and A. Raefsky, Anelastic response of the earth to a dip slip earthquake, *J. Geophys. Res., 88*, 515-525, 1983.

Pacheco, J. F., L. R. Sykes, and C. H. Scholz, Nature of seismic coupling along simple plate boundaries of the subduction type, *J. Geophys. Res., 98*, 14,133-14,159, 1993.

Rice, J. R., The mechanics of earthquake rupture, in *Physics of the Earth's Interior*, edited by A. M. Dziewonski and E. Boshi, pp. 555-649, North-Holland, New York, 1980.

Rice, J. R., and W. D. Stuart, Stressing in and near a strongly coupled subduction zone during the earthquake cycle (abstract), *Eos, Trans, AGU, 70* (43), 1063, 1989.

Ruff, L., and H. Kanamori, Seismic coupling and uncoupling at subduction zones, *Tectonophysics, 99*, 99-117, 1983.

Rundle, J. B., A physical model for earthquakes, 1, Fluctuations and interactions, *J. Geophys. Res., 93*, 6237-6254, 1988a.

Rundle, J. B., A physical model for earthquakes, 2, Applications to Southern California, *J. Geophys. Res., 93*, 6255-6274, 1988b.

Savage, J. C., A dislocation model of strain accumulation and release at a subduction zone, *J. Geophys. Res., 88*, 4984-4996, 1983.

Savage, J. C., Interseismic uplift at the Nankai subduction zone, *J. Geophys. Res., 100*, 6,339-6,350, 1995.

Savage, J. C., M. Lisowski, and W. H. Prescott, Strain accumulation in western Washington, *J. Geophys. Res., 96*, 14,493-14,507, 1991.

Stuart, W. D., Forecast model for great earthquakes at the Nankai Trough subduction zone, *Pure Appl. Geophysics, 126*, 619-641, 1988.

Thatcher, W., and J. B. Rundle, The earthquake deformation cycle and the Nakai Trough, south-west Japan, *J. Geophys. Res., 89*, 3087-3101, 1984a.

Thatcher, W., and J. B. Rundle, A viscoelastic coupling model for the cyclic deformation due to periodically repeated earthquakes at subduction zones, *J. Geophys. Res., 89*, 7631-7640, 1984b.

Tse, S. T., and J. R. Rice, Crustal earthquake instability in relation to the depth variation of frictional slip properties, *J. Geophys. Res., 91*, 9452-9472, 1986.

Wahr, J., and M. Wyss, Interpretation of postseismic deformation with a viscoelastic relaxation model, *J. Geophys. Res., 85*, 6471-6477, 1980.

Zheng, G., R. Dmowska, and J. R. Rice, Modeling earthquake cycles in the Shumagins subduction segment, Alaska, with seismic and geodetic constraints, *J. Geophys. Res.*, this issue.

R. Dmowska, J. R. Rice, M. A. J. Taylor, and G. Zheng, Division of Applied Sciences and Department of Earth and Planetary Sciences, Harvard University, Pierce 327, 29 Oxford Street, Cambridge, MA 02138. (e-mail: dmowska@geophysics.harvard.edu; rice@esag.harvard.edu; taylor@husm.harvard.edu; zheng@husm.harvard.edu)

W. D. Stuart, U. S. Geological Survey, Menlo Park, CA 94025. (e-mail: stuart@samoa.wr.usgs.gov)

(Received May 31, 1995; revised November 9, 1995;
accepted November 16, 1995.)